Seasonal Heat and Salt Balance in the Upper Gulf of California

Authors: Montes, Jorge M., Lavín,, Miguel F., and Parés-Sierra, Alejandro F.

Source: Journal of Coastal Research, 32(4) : 853-862

Published By: Coastal Education and Research Foundation

URL: https://doi.org/10.2112/JCOASTRES-D-14-00192.1

Journal of Coastal Research	32	4	853–862	Coconut Creek, Florida	July 2016

Seasonal Heat and Salt Balance in the Upper Gulf of California

Jorge M. Montes*, Miguel F. Lavín, and Alejandro F. Parés-Sierra

Departamento de Oceanografía Física
CICESE
Ensenada, Baja California, México

www.cerf-jcr.org

www.JCRonline.org

ABSTRACT

Montes, J.M.; Lavín, M.F., and Parés-Sierra, A.F., 2016. Seasonal heat and salt balance in the Upper Gulf of California. *Journal of Coastal Research,* 32(4), 853–862. Coconut Creek (Florida), ISSN 0749-0208.

The salinity and heat balance, as well as the seasonal variation of the average absolute salinity ($\langle S_A \rangle$) and conservative temperature ($\langle \Theta \rangle$), were described by using data from 24 cruises within four domains in the Upper Gulf of California (UGC). Monthly values of S_A and Θ, and surface fluxes obtained from ERA-Interim reanalysis data sets were fitted to a seasonal signal, and the horizontal fluxes of salinity and heat content were calculated by using balance equations. The UGC exports salt and heat to the Northern Gulf of California (NGC) almost all year, with an annual mean of 1.6 g/kg per year for the salinity flux and 0.16 terawatts (TW) for the heat flux. The results suggest that the net excess of evaporation (~0.8 m/y) and heat gain by the surface (~70 W/m^2) are the main factors controlling the exchange of salinity and heat between the UGC and the NGC. To help identify the relevant dynamic factor involved in the heat and salinity balances, a high-resolution numerical model, the regional ocean modeling system (ROMS), was implemented for the region. The main feature of the UGC circulation consists of a cyclonic surface flow that extends downward as a laterally sheared flow pattern, with inflow at the Sonora coast side and outflow at the Baja California coast side. Although the cyclonic circulation pattern remains most of the year, the maximum velocities (~0.20 m/s) are reached in June. The results indicate that the major exchange between the UGC and the NGC occurs in June and July when the net volume transport (~0.9 Sverdrups) is dominated by the horizontal overturning transport.

ADDITIONAL INDEX WORDS: *Salinity balance, heat balance, circulation, transport.*

INTRODUCTION

The Upper Gulf of California (UGC) is a shallow (<30 m depth) embayment at the head of the Gulf of California (Figure 1); it is a highly seasonal, macrotidal inverse estuary, with temperatures ranging from ~14°C in winter to >32°C in summer (Alvarez-Borrego, Flores-Báez, and Galindo-Bect, 1975; Alvarez-Borrego and Galindo-Bect, 1974; Lavín, Godnez, and Alvarez, 1998). The damming of the entire Colorado River flow, the high evaporation rate (~0.9 m/y), and the almost null precipitation are the origins of the inverse estuarine conditions that exist today in the UGC, characterized by salinities that increase from 35.4 g/kg in the open Northern Gulf to >39 g/kg in the shallowest areas (Alvarez-Borrego, Flores-Báez, and Galindo-Bect, 1975; Lavín, Godínez, and Alvarez, 1998; Lavín and Organista, 1988; Lavín and Sánchez, 1999). The tidal range is ~6 m during spring tides, and strong tidal currents, up to 1 m/s, in addition to a tidal mixing front separating the well-mixed UGC, form the deeper and stratified Northern Gulf (Argote *et al.*, 1995).

The heat fluxes in the Gulf of California (GC) have a strong seasonal signal (Castro, Lavín, and Ripa, 1994). The seasonal variation of the mean salinity and heat content in the GC are controlled mainly by the salinity and heat exchanges at the boundary between the GC and the Pacific Ocean; these exchanges dominate the seasonal variation produced by the exchanges of heat and moisture with the atmosphere (Beron-Vera and Ripa, 2000, 2002; Castro, Lavín, and Ripa, 1994). In the northern GC (NGC), the net seasonal surface heat flux includes heat loss (cooling) during winter (Beron-Vera and Ripa, 2000; Lavín and Organista, 1988; Paden, Winant and Abbott, 1993).

Despite the harsh conditions, the UGC remains a spawning and nursery habitat for many species of fishes (Sánchez-Velasco *et al.*, 2012). Additionally, it is home to the most endangered marine cetacean, the vaquita (*Phocoena sinus*), a species endemic to the UGC. Great efforts are being made to try to save the vaquita from extinction, in terms of both basic physical oceanography and biology, as well as through managerial measures.

One of the great unknowns about the UGC is its circulation. Because there are no data available, numerical models are being used to study it (Marinone, 2003). Among the possible forcing agents are the buoyancy flux and circulation outside the UGC, specifically in the Northern Gulf (Figure 1).

The seasonal circulation in the NGC has been well documented with geostrophic velocity calculations (Carrillo, Lavín, and Palacios-Hernández, 2002), moored current meters, and surface drifters (Palacios-Hernández *et al.*, 2002). This circulation is dominated by a seasonal eddylike circulation: cyclonic from June to September and anticyclonic from November to April. A three-dimensional numerical model of the seasonal circulation of the GC by Marinone (2003) and Marinone, Lavín, and Parés-Sierra (2011) shows that the large-scale circulation influences the NGC, but it does not resolve the UGC well.

DOI: 10.2112/JCOASTRES-D-14-00192.1 received 7 October 2014; accepted in revision 8 March 2015; corrected proofs received 10 April 2015; published pre-print online 5 May 2015.
*Corresponding author: jmontes@cicese.edu.mx

The aim of this work is to investigate the seasonal circulation and the seasonal balances of heat and salt in the UGC. We used historical hydrographic data to calculate the heat and salt content variation, and we obtained the net surface heat flux from ERA-Interim data. To study the seasonal circulation, we used a high-resolution nested regional ocean modeling system (ROMS) model.

METHODS

In situ data from 24 cruises made in the UGC between 1973 and 2010 were used to calculate the conservative temperature (Θ, °C) and absolute salinity (S_A, g/kg) with the TEOS-10 Gibbs-Seawater Oceanographic Toolbox (McDougall and Barker, 2011). After eliminating the data from El Niño years, monthly averages of the variables were calculated to construct an annual cycle; there were no cruises in April.

To calculate the monthly net surface heat flux Q, we used the monthly means of latent heat flux, sensible heat flux, shortwave radiation, and long-wave radiation from the monthly means of the ERA-Interim analysis obtained from the European Centre for Medium-Range Weather Forecasts data server (ECMWF, 2010). The evaporation rate E was obtained from the latent heat flux: $E = Q_e/\rho_w L_v$, where ρ_w is the density of fresh water, and L_v is the latent heat of evaporation.

The S_A and Θ data were interpolated to a regular grid by objective mapping. To calculate the bulk heat and salt balance, three domains (D1, D2, and D3) were selected because they had the best time and space data coverage. The data from each grid element were averaged vertically and horizontally to obtain the mean values in the three domains.

To smooth out the variability produced by using data from different years and to fill in the missing months, the seasonal signal (annual and semiannual) was obtained by a nonlinear least-squares fit applied to the monthly means of temperature, salinity, surface heat, and moisture fluxes for each domain:

$$F(t) = A_0 + A_1\cos(\omega t - \varphi_1) + A_2\cos(2\omega t - \varphi_2), \qquad (1)$$

where t is the month of the year, and ω is one cycle per year. The fitted data are presented with 95% prediction bounds.

Heat and Salinity Balance Equations

Following Beron-Vera and Ripa (2002), the average salinity and temperature inside a volume $V(t)$ surrounded by a boundary $\Gamma(t)$ is given by

$$\langle S_A\rangle = \frac{1}{V}\iiint_V S_A dV \qquad (2)$$

and

$$\langle \Theta\rangle = \frac{1}{V}\iiint_V \Theta dV, \qquad (3)$$

and considering the common incompressibility approximation, $\nabla\cdot\boldsymbol{u} = 0$, their variation in time is given by

$$V\frac{d\langle S_A\rangle}{dt} = \oint_\Gamma \left[S'_A(\boldsymbol{u}-\boldsymbol{u}_\Gamma) - \kappa_S\nabla S_A\right]\boldsymbol{n}\,da \qquad (4)$$

and

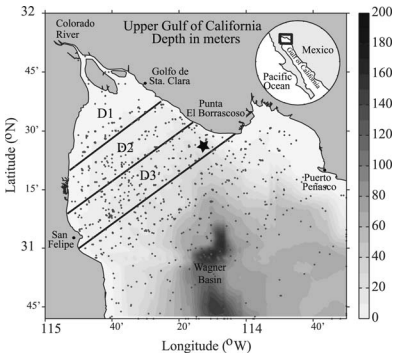

Figure 1. Map of the Upper Gulf of California with bathymetry in meters and the locations of hydrographic casts (black dots). The solid lines delimit the domains in which the data were simplified for the study of the seasonal heat and salinity balances. The star symbol indicates the location where the ADP current meter was moored in summer 1999.

$$V\frac{d\langle\Theta\rangle}{dt} = \oint_\Gamma \left[\Theta'(\boldsymbol{u}-\boldsymbol{u}_\Gamma) - \kappa_\Theta\nabla\Theta\right]\boldsymbol{n}\,da, \qquad (5)$$

where κ_S and κ_Θ are coefficients of the diffusivity of salt and heat, respectively; $S'_A = (S_A - \langle S_A\rangle)$ and $\Theta' = (\Theta - \langle\Theta\rangle)$; and $\boldsymbol{u}_\Gamma$ is the velocity at the boundary. The unitary normal vector in that surface is $\boldsymbol{n}$, and da is the area differential.

The boundary Γ can be divided into two parts, one (Γ^B) corresponding to the coast, the bottom, and the vertical boundaries between domains; and the other (Γ^S) corresponding to the sea surface. At the Γ^S boundary, we use the kinematic boundary condition for mass transport through the sea surface as proposed by Krauss (1973) and Beron-Vera, Ochoa, and Ripa (1999), and later used by Beron-Vera and Ripa (2000, 2002) for the salt and heat balances in the GC. Evaporation (E) implies a loss of fresh water, and precipitation (P) is a source of fresh water; thus, the difference in the normal velocities at the boundary Γ^S is proportional to the mass transport through the boundary. Additionally, the heat fluxes through the ocean surface were considered for the heat balance, with the condition $\rho C_p\kappa_\Theta\nabla\Theta\cdot\boldsymbol{n} = Q$.

At the Γ^B boundary, only the flows between the domains are nonzero, because in the rest of the boundary, the velocity normal to the surface $\boldsymbol{u}\cdot\boldsymbol{n} = 0$. Additionally, considering that the bottom boundary is fixed, the velocity in that part of the boundary $\mathbf{u}^B_\Gamma = 0$. Under these considerations, the balance equations for salinity and heat content are

$$V\frac{d\langle S_A\rangle}{dt} = \oint_{\Gamma^S}[\langle S_A\rangle(E-P)]da^s - \oint_{\Gamma^B}\left[S'_A\boldsymbol{u} - \kappa_S\nabla S_A\right]\boldsymbol{n}^F da^F \qquad (6)$$

and

$$\rho C_p V\frac{d\langle\Theta\rangle}{dt} = \oint_{\Gamma^s}\left[Q - \rho C_p\Theta(E-P)\right]da^s - \rho C_p\oint_{\Gamma^B}[\Theta'\mathbf{u} - \kappa_\Theta\nabla\Theta]\boldsymbol{n}^F da^F, \qquad (7)$$

respectively; these are simplified as

$$F^S = \langle S_A \rangle (E-P)A - V\frac{d\langle S_A \rangle}{dt} \quad (8)$$

and

$$F^{\mathrm{H}} = \left[Q - \rho C_p \langle \Theta \rangle (E-P)\right]A - \rho C_p V \frac{d\langle \Theta \rangle}{dt}, \quad (9)$$

where F^{S} and F^{H} are the advective plus diffusive salinity anomaly (S') flux and the heat content anomaly $\rho C_p \Theta'$ fluxes at the boundary I^{B}, respectively; ρ, C_p, V, A, $\langle S \rangle$, $\langle \Theta \rangle$, $(E-P)$, and Q are the density, heat capacity coefficient, volume, vertical area, average salinity, average temperature, evaporation minus precipitation, and net heat flux, respectively.

The horizontal fluxes between the vertical boundaries of the domains can be calculated by using balance Equations (8) and (9). From the boundary conditions previously explained, the total flux F_i at the boundary I^{B} of each domain D_i ($i = 1, \ldots, 3$) is equal to the sum of the fluxes across the vertical boundaries between domains (i.e., the flux across the northern boundary $F_{i-1/2}$ and the flux at the southern boundary $F_{i+1/2}$; positive outward). With this notation, the fluxes of S'_{A} and $\rho C_p \Theta'$ between the domains can be obtained as

$$F^{\mathrm{S}}_{i+1/2} - F^{\mathrm{S}}_{i-1/2} = \langle S_{\mathrm{A}} \rangle_i A_i (E-P)_i - V_i \frac{d\langle S_{\mathrm{A}} \rangle_i}{dt} \quad (10)$$

and

$$F^{\mathrm{H}}_{i+1/2} - F^{\mathrm{H}}_{i-1/2} = \left[Q_i - \rho_i C_{p_i} \langle \Theta \rangle_i (E-P)_i\right]A_i - \rho_i C_{p_i} V_i \frac{d\langle \Theta \rangle_i}{dt}. \quad (11)$$

Given the boundary condition $F_{1/2} = 0$ (at the head of the UGC), the above equations are algebraic systems closed with respect to the three unknown fluxes $F_{i+1/2}$. The following values of V_i were used to solve the system: $V_1 = 7.20 \times 10^9$ m^3, $V_2 = 2.20 \times 10^{10}$ m^3, $V_3 = 4.07 \times 10^9$ m^3. Additionally, C_p and ρ, were calculated with the TEOS-10 Toolbox using conservative temperature and absolute salinity data.

In this work, the interannual variability was not considered; interannual variability contaminates the seasonal fit because not all months are equally sampled. Parameters like surface area or volume of each box may strongly affect the estimation of the horizontal heat and salt fluxes. For this reason, we try to be as cautious as possible when getting estimates of these parameters. The surface area was obtained using the polygon formed by the coastline and the boundary between the domains. This is a numerical estimate using a line integral based on Green's Theorem. As such, it is limited by the accuracy and resolution of the data; in this case the full-resolution global self-consistent, hierarchical, high-resolution geography coastline data set was used (Wessel and Smith, 1996).

Numerical Model

A nested configuration of the ROMS for the NGC within a larger configuration covering the entire GC was used to study the circulation in the UGC. The nested domain had a spatial resolution of ~1 km with 20 vertical sigma layers distributed according to the following stretching parameters: theta_s = 6, theta_b = 0.2, and hc = 5. Small-scale processes were parameterized by the nonlocal K-profile scheme (Large, McWilliams, and Doney, 1994). Horizontally, a Laplacian mixing coefficient of 30 m^2/s was used, whereas no extra mixing for tracers was used. Climatological heat fluxes from the Comprehensive Ocean-Atmosphere Data Set (Woodruff *et al.*, 1987) and climatological averages from both the 10-m wind field from the North America Regional Reanalysis (Mesinger *et al.*, 2006) and the advanced very high resolution radiometer (AVHRR)–Pathfinder sea surface temperature (Casey *et al.*, 2010) were included as atmospheric forcing. Sea surface height, temperature, salinity, and horizontal velocity fields from the Simple Ocean Data Assimilation database (Carton and Giese, 2008) were used as open-ocean boundary conditions for the large model (GC). The sea floor bathymetry was derived from the ETOPO1 dataset (Amante and Eakins, 2009) and corrected with *in situ* bathymetric measurements on the UGC region. The NGC model was forced at the lateral boundaries by the GC model. Tides were included in the larger configuration by using the TPSX06 model (Egbert and Erofeeva, 2002) and were transmitted to the nested domain as part of the boundary conditions. ROMSTOOLS software routines (Penven *et al.*, 2008) were used to generate the forcing fields, bathymetry, and initial and boundary conditions suitable for the ROMS nesting implementation.

The model takes approximately 4 y to reach the spin-up of the solution and to obtain statistical equilibriums. The sample interval is 6 h. After the model reaches spin-up, we take the monthly mean of the last year.

RESULTS

The results of the nonlinear least-squares fit were used to provide a description of the seasonal variation of the hydrographic variables and surface heat fluxes and to calculate the terms of the balance equations of heat and salt in the UGC. The results of the implementation of a high-resolution numerical model (ROMS) in the region were used to help identify the relevant dynamic factor involved in the heat and salinity balances and to obtain a detailed description of the circulation within the UGC.

Surface Fluxes

The total net surface heat flux (Figure 2a) in the UGC shows a gain of heat by the ocean from January to October and a net loss in November and December. The annual mean of the net surface heat flux Q in the UGC is 70.64 W/m^2. The annual component has an amplitude of 103.28 W/m^2 and explains 92.30% of the total variance. The maximum value in the annual cycle is recorded in June. The semiannual component has an amplitude of 16.44 W/m^2 and explains only 2.28% of the variability. The semiannual cycle reaches its maxima in April and October (Table 1).

Evaporation always exceeds precipitation in the UGC (Figure 2b), with an annual mean of 0.82 m/y. The seasonal adjusted results show that the variability of $E-P$ is dominated by the annual component, which has an amplitude of 0.35 m/y and explains 83.30% of the total variability; the annual cycle reaches its maximum value in September. The semiannual component has an amplitude of 0.10 m/y and explains only

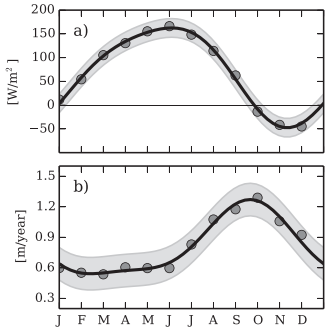

Figure 2. Seasonal fit (solid curves) of (a) net heat flux Q and (b) $E - P$. The dots represent the monthly means of the data; the shaded band corresponds to the 95% prediction bounds.

6.72% of the total variability; the semiannual cycle reaches its maximum values in January and July (Table 1).

Seasonal Salinity Balance

The results of the seasonal fit to the monthly values of S_A are shown in Table 2 and in Figures 3a–c. The annual mean of S_A decreases from 36.74 g/kg at domain D1 (at the head of the UGC) to 36.04 g/kg at domain D3. The annual amplitude has a maximum of 0.63 g/kg at domain D1 and decreases to 0.15 g/kg at domain D3. The maximum value in the annual cycle occurs between August and September in all the domains. The average salinity also shows an important semiannual component, with amplitudes on the same order as annual values, except in domain D1, where the amplitude of the semiannual component is almost negligible compared with the annual amplitude. The maximum value in the semiannual cycle occurs in May/November at domain D1 and between July/February and September/March at domains D2 and D3, respectively.

The explained variance shows that in domains D1 and D2, the annual component dominates the variability, accounting for 66.02% and 83.71% of the total variability, respectively. The semiannual component in these two domains explains only a small part of the variability, almost 1% in domain D1 and 12% in domain D2. In domain D3, the annual and semiannual components explain almost the same percentage of the variability, and the two components together explain 46.68% of the variability.

The horizontal salinity anomaly flux across the vertical boundary between domains D_i and D_{i+1} (*i.e.* $F_{i+1/2}$) (Figure 3d), shows that the UGC exports salt throughout the year. The annual mean of the salinity anomaly flux increases almost linearly from zero at the head of the UGC (*i.e.* no flux at the head) to 1.60 g/kg per year at the mouth of the UGC. This flux has an important annual variation, with a minimum amplitude of 0.91 g/kg per year at domain D1, increasing almost linearly to 2.31 g/kg per year at domain D3. The phase of the annual amplitude indicates that the annual cycle of the salinity anomaly flux reaches its maximum in November. The semiannual amplitude also increases toward the mouth from 0.24 g/kg per year at domain D1 to 1.50 g/kg per year at domain D3. The semiannual maxima occur in May and September in all the domains.

The global balance in the UGC is shown in Figure 3e. The part due to $E - P$ (black line) is positive throughout the year, with a maximum of 2.37 g/kg per year in October and remaining almost constant from February to March. The change in average salinity (gray line) reaches its maximum value of 2.32 g/kg per year in September. The difference between the terms due to $E - P$ and the total average salinity change divided by the total volume represents the total salinity anomaly flux through the mouth of the UGC (dashed line); a strong output of salinity is present, with a maximum of 5.32 g/kg per year reached in November. In May, there is another output, with a maximum of 0.71 g/kg per year. Two inputs are presented in the year: one in March with a maximum of 0.32 g/kg per year and another in August with a maximum of 0.52 g/kg per year.

Seasonal Heat Balance

The results of the seasonal fit to the monthly values of Θ are shown in Table 3 and in Figures 4a–c. The annual mean temperature (Θ) decreases from 21.58°C at domain D1 to 22.40°C at domain D3. The annual amplitude has a maximum of 8.75°C at domain D1 and decreases to 6.98°C at domain D3. The maximum value in the annual cycle occurs between July and August in all the domains. The semiannual cycle is smaller than the annual cycle by almost one order of magnitude. The maximum value in the semiannual cycle occurs in June/January at domain D1 and in May/November at domains D2 and D3.

The explained variance shows that the annual component dominates the temperature variability in the UGC; it explains 87.17% of the variability in domain D1, 85.68% in domain D2, and 83.33% in domain D3. The semiannual component accounts for only a small part of the total variability, explaining 4.84% in domain D1, 3.43% in domain D2, and 0.91% in domain D3.

The horizontal heat content anomaly flux across the vertical boundary between domains (Figure 4d) shows that the UGC exports heat throughout the year. The annual mean of the horizontal heat content anomaly flux increases almost linearly from zero at the head of the UGC to 0.16 terawatts (TW) at its mouth. This flux has an important annual variation, with a minimum amplitude of 0.08 TW at domain D1 increasing almost linearly to 0.18 TW at domain D3. The phase of the annual amplitude indicates that the annual cycle of the heat content anomaly flux reaches its maximum between October and November in domains D1 and D2 and in August in domain D3.

Table 1. *Result of the seasonal fit of evaporation minus precipitation (*E − P*) and net heat flux (*Q*) in the UGC.*

	A_0	A_1	A_2	φ_1 (mo)	φ_2 (mo)	Var_1 (%)	Var_2 (%)
Q (W/m^2)	70.64 ± 2.37	103.28 ± 3.36	16.44 ± 3.36	5.55	4.05	92.30	2.28
$E - P$ (m/y)	0.82 ± 0.01	0.35 ± 0.27	0.10 ± 0.02	9.55	7.54	83.30	6.72

Table 2. *Result of the seasonal fit of the absolute salinity for each domain.*

	A_0 (g/kg)	A_1 (g/kg)	A_2 (g/kg)	φ_1 (mo)	φ_2 (mo)	Var_1 (%)	Var_2 (%)
D1	36.74 ± 0.11	0.63 ± 0.15	0.07 ± 0.14	9.33	5.73	66.02	0.91
D2	36.37 ± 0.04	0.41 ± 0.06	0.15 ± 0.07	9.00	7.78	83.71	12.04
D3	36.04 ± 0.07	0.15 ± 0.10	0.13 ± 0.11	8.85	9.84	25.91	20.77

The global heat balance for the entire UGC is shown in Figure 4e. The part due to the surface fluxes (black line) shows a net gain of heat throughout the surface from February to September, with a maximum of 0.53 TW in June and a net loss in the rest of the year, with a maximum of 0.29 TW in November. The rate of change of the average heat content (gray line) shows that heating takes place from January to August, with a maximum of 0.42 TW in June. The total heat content anomaly flux shows an input of heat through the mouth of the UGC from December to March, with a maximum of 0.07 TW. Output is stronger the rest of the year, with a maximum of 0.43 TW in November.

Surface Circulation

The monthly mean surface currents obtained with the ROMS in the NGC (presented in the Supplementary Material) show that the main dynamic feature is a seasonally reversing eddy: cyclonic from May to October, with a maximum speed of ~0.5 m/s, and anticyclonic from November to March, with a maximum velocity of ~0.20 m/s. The summer cyclonic eddy is larger, stronger, and much better defined than the winter anticyclonic eddy.

The monthly circulation in the UGC (Figures 5a–l) reveals a seasonal variation that seems to be strongly affected by the circulation in the NGC. From March to July, a cyclonic flow dominates the circulation in the UGC, with inflow on the mainland side and outflow on the peninsular side; these currents have a maximum speed of ~0.20 m/s. The anticyclonic circulation pattern lasts until December, with currents moving at a maximum speed of ~0.15 m/s. In January and February, there is no well-defined pattern of circulation, and the currents reach a minimum speed of ~0.03 m/s. The annual mean of surface currents (Figure 5m) shows a cyclonic circulation, with some variable direction flows south of San Felipe in the mainland half of the Upper Gulf.

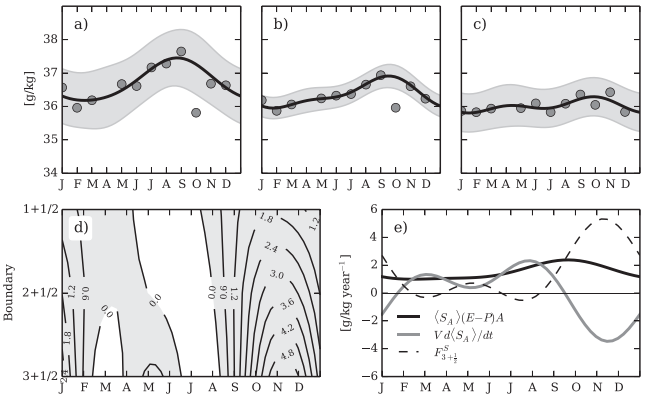

Figure 3. Seasonal fit (solid curve) of (S) in domains D1 (a), D2 (b), and D3 (c). The dots represent the monthly means of the data; the shaded band corresponds to the 95% prediction bounds. (d) Horizontal salinity anomaly flux across domain boundaries. (e) Seasonal salinity balance in the UGC; the lines represent each term of the salinity balance equation.

Model and ADP Mooring Velocity Comparison

Figure 6 shows a comparison of modeled residual currents and observed full water column residual currents from a bottom-mounted acoustic Doppler current profiler (ADP), deployed during summer 1999 (Figure 1). Tide variability was filtered using the PL64 filter described in Beardsley, Limburner, and Rosenfeld (1985). At the mooring location, the low-pass filtered ADP data (Figure 6a) shows that, during neap tides, the surface currents are directed inward at a maximum of ~0.06 m/s above 15 m, whereas deeper waters flow outward at a maximum of ~0.05 m/s. This inverse estuarine-like restitution flow has a fortnightly modulation driven by neap tides and lasts between 7 and 10 days. In the modeled residual currents (Figure 6b), although the temporal variability is well captured, including the gravity current events during neap tides, the inward and outward flows are underestimated.

Vertical Distribution of Velocity

The velocity perpendicular to the boundary between domain D3 and the NGC shows a strong horizontally sheared pattern from March to August (Figures 7c–h). This pattern consists of a superficial inflow that extends almost through the entire water column, narrowing on the mainland side and with an outflow on the peninsular side. The outflow on the peninsular side is restricted to a smaller part at the surface compared with the inflow. This pattern in the vertical distribution of velocity is also observed in the annual average (Figure 7m). From September to October, the cyclonic pattern diminishes, leading to a more complex pattern with alternating cores of inflow and outflow from November to February. The maximum speed of inflow is observed in June, at ~0.2 m/s near the surface. The same applies to the outflow, with a maximum speed of ~0.2 m/s near the depth of 10 m.

Transport

The vertical distribution of velocity suggests a strong basin-scale horizontal overturning circulation consisting of a northwestward inflow on the mainland side and a southeastward outflow on the peninsular side. One way to describe this circulation is by calculating the volume transport with the vertical and horizontal integrated velocity perpendicular to the transect.

The vertical integrated transport (Figure 8a) shows that, from March to August, the transport associated with the inflow (positive) is concentrated near the deepest part of the transect, next to the coast of Sonora, and the transport associated with the outflow (negative) extends widely across the width of the transect. This feature was expected because of the strong cyclonic circulation present during this period. The same

Table 3. *Result of the seasonal fit of the temperature for each domain.*

	A_0 (°C)	A_1 (°C)	A_2 (°C)	φ_1 (mo)	φ_2 (mo)	Var_1 (%)	Var_2 (%)
D1	21.58 ± 0.61	8.75 ± 0.81	2.06 ± 0.81	7.06	6.15	87.17	4.84
D2	21.96 ± 0.44	7.77 ± 0.59	1.55 ± 0.59	7.39	4.81	85.68	3.43
D3	22.40 ± 0.46	6.98 ± 0.62	0.74 ± 0.61	7.75	5.22	83.33	0.95

finding is observed during September and October, the difference being that the core of the positive transport moves toward the deepest part. The maximum transport, both positive and negative, is reached in June at 0.03 Sverdrups (SV).

The horizontal integrated transport (Figure 8b) shows that the transport distribution changes direction with depth. In the period when the cyclonic circulation is predominant (March to August), the inflow transport is present from the surface to 10 m of the water column, and the outflow transport from 10 m to the bottom. In September and October, this pattern seems to be reversed, with outflow at the surface and inflow below 20 m. The maximum values, both positive and negative, are reached in July at 0.01 SV.

The above results show that the exchange between the NGC and the UGC is mainly horizontal. This is most evident in the net transport (Figure 8c), which shows that, in the period of maximum exchange, the net horizontal transport is up to four times larger than the net vertical transport. This was expected because of the strong laterally sheared exchange flow observed in the velocity field.

The above exchange mechanism should be reflected in the hydrographic conditions within the UGC; to verify this, we used data from a hydrographic survey done in the UGC in June 2010.

The horizontal distribution of the hydrographic variables shows that the surface salinity (Figure 9a) increases toward the northwest, where the maximum salinity (~37.5 g/kg) is found in a narrow high-salinity tongue close to the Baja California (BC) coast, and the minimum salinity (~35.8 g/kg) is recorded at the southeast. This distribution is also observed in the surface density (Figure 9b), with the maximum density (~25 kg/m^3) close to the BC coast and the minimum density (~24 kg/m^3) at the southeast. The shape of the 36 and 35.8 g/kg isohalines south of Punta Borrascoso suggests an intrusion of offshore water toward the UGC, which is also apparent in the surface isopycnals in that area.

To complete the description, vertical sections close to the southern boundary of domain D3 are also presented. The vertical distribution shows that the salinity (Figure 9c) is almost vertically mixed; hence, the high-salinity tongue close the BC coast and the less saline water intrusion observed at the surface are present throughout the water column, with a value of 36 g/kg in the east increasing to 37 g/kg in the west. The vertical distribution of density (Figure 9d) shows a slightly lateral front, with denser water (~25 kg/m^3) extending across the bottom and less dense water at the surface (~24.6 kg/m^3); this pattern may be associated with the inflow of less dense water at the surface and the outflow of denser water at the bottom.

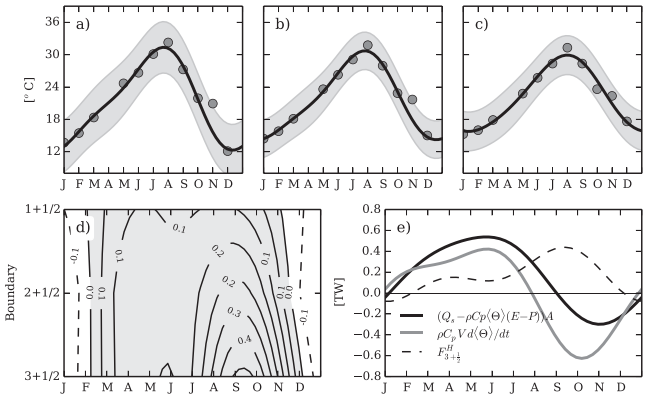

Figure 4. Seasonal fit (solid curve) of Θ in domains D1 (a), D2 (b), and D3 (c). The dots represent the monthly means of the data; the shaded band corresponds to the 95% prediction bounds. (d) Horizontal heat content anomaly flux across domain boundaries. (e) Seasonal heat balance in the UGC; the lines represent each term of the heat content balance equation.

DISCUSSION

The result of the seasonal fit of the net heat flux agrees with those previously obtained by Lavín and Organista (1988), who reported an annual mean of 69.3 W/m^2, calculated by using sea surface temperature observations and 1979–1986 data from a meteorological station in Puerto Peñasco. However, the results differ from those reported by Castro, Lavín, and Ripa (1994), who obtained 80.4 W/m^2 in the region of the UGC.

The evaporation rate obtained from the latent heat flux from ERA-Interim data compares well with those previously obtained: Bray (1988b) and Lavín and Organista (1988) reported an annual mean of 0.9 m/y; Beron-Vera and Ripa

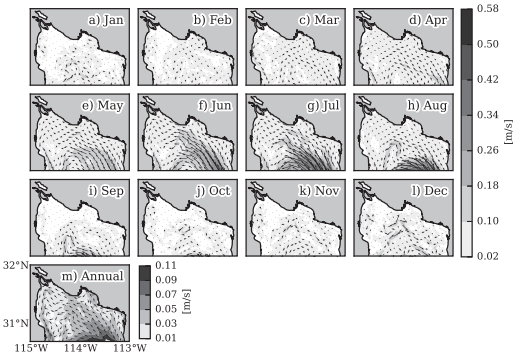

Figure 5. (a–l) Monthly mean surface currents obtained with the ROMS in the UGC. Contours represent the speed (m/s); the arrows indicate the direction of the current. (m) Annual mean surface currents; the arrows in the annual mean are normalized to the same length.

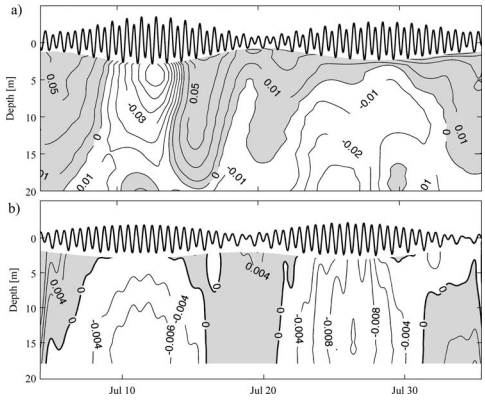

Figure 6. Time series of currents across the mouth of the UGC at the location marked in Figure 1: (a) low-pass–filtered data from a bottom-mounted ADP and (b) low-pass–filtered currents from ROMS.

(2002) obtained 0.6 m/y by using monthly time series meteorological data from 1961 to 1986.

The highest values of salinity are found at the head of the UGC; the annual mean of the average salinity in domain D1 is almost 1 g/kg higher than in domain D3. The high evaporation rate in the NGC is a mechanism that produces high-salinity water (Bray, 1988a; Lavín *et al*., 1995; Lavín, Godínez, and Alvarez, 1998). The loss of freshwater from the high evaporation rate in the UGC induces an influx of water from the NGC that increases the salinity in the UGC. This excess of salinity (S_A) over the average salinity ($\langle S_A \rangle$) (*i.e*. the salinity anomaly) must be exported out of the UGC to attain balance. Unlike the GC, where the global salt balance is dominated by interaction with the Pacific Ocean (Beron-Vera and Ripa, 2002), the excess of evaporation and the change in salinity in the UGC are of the same order of magnitude. Besides the differences between the GC and the UGC in the global balance, the salinity anomaly transport obtained in this work (0.005 SV g/kg) agrees with

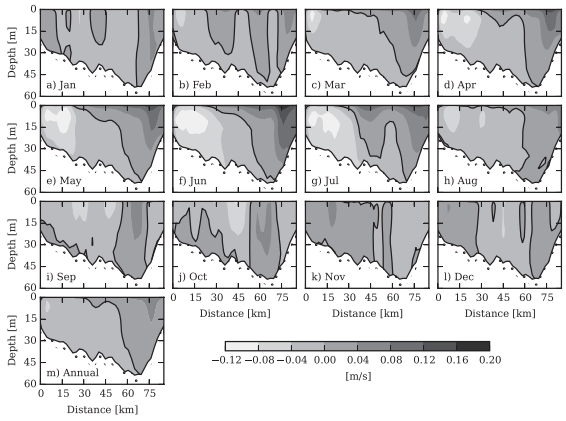

Figure 7. Monthly (a–l) and annual (m) means of the vertical distribution of velocity for the boundary between domain D3 and the NGC; the contours correspond to the velocity (m/s).

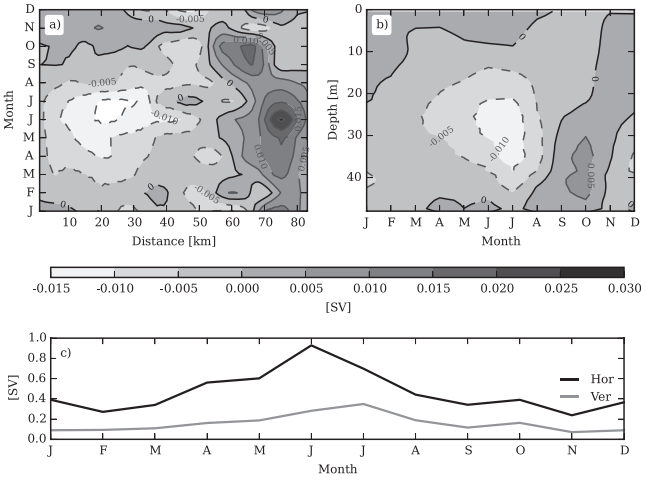

Figure 8. Vertical (a) and horizontal (b) integrated transport. (c) Integrated vertical (black line) and horizontal (gray line) transport at the transect located at the boundary of the UGC and the NGC.

that obtained by (Beron-Vera and Ripa, 2002) at the nearest border to the UGC (0.01 SV PSU). The maximum of the anomaly flux occurs 1 month after the $E - P$ reaches its maximum value. As in any inverse estuary, the change in the local salinity is influenced primarily by evaporation. The influx of salt caused by the consistent fresh water lost by evaporation will increase the salinity within the UGC; this implies a compensating seaward efflux of salt with similar magnitude. It is possible to relate the phase lags between these two fluxes with the salt flushing time. According to de Silva Samarasinghe and Lennon (1987), flushing time is the ratio of the excess of salt content over a background or a base level to the salt efflux. Using the mean salinity (S_i) and efflux ($F_{i+1/2}$) values of each box (D_i) defined within the UGC, the flushing

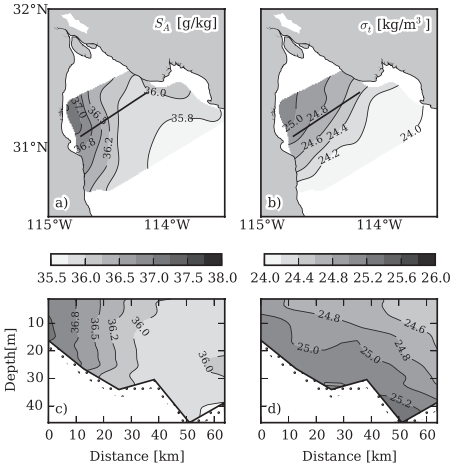

Figure 9. Surface hydrography: (a) absolute salinity (g/kg) and (b) density (kg/m^3). Vertical distribution of hydrographic variables along the transect (black line): (c) absolute salinity (g/kg) and (d) density (kg/m^3).

times vary from 30 days for D1 to 89 days for D2 and 100 days for D3. From Figure 3 it is seen that the lags between $F_{i+1/2}$ and $[S_i A(E-P)]$, are consistent with the flushing time obtained for each domain.

Circulation

The ROMS configuration adequately reproduces the circulation previously reported by Carrillo, Lavín, and Palacios-Hernández (2002), Lavín *et al*. (1997), and Palacios-Hernández *et al*. (2002) in the NGC. The transition periods found by Carrillo, Lavín, and Palacios-Hernández (2002) and by Palacios-Hernández *et al*. (2002) are around October and April–May and are characterized by the simultaneous presence of both types of gyres; in this work, the transition periods are found in March and November.

In the UGC, the model reproduces well the residual circulation observed in summer from ADP mooring data. The main dynamic feature consists of gravity current events modulated by the spring-neaps cycle. During spring tides, the turbulent kinetic energy (TKE) from the tidal flow maintains vertically mixed conditions, and its effect on the gravity current is similar to a very high friction coefficient, so that the gravitational circulation is inhibited. During neap tides, the TKE cannot maintain vertically mixed conditions, and the dense coastal water sinks and flows down the bottom gradient as a gravity current (Nunes-Vaz, Lennon, and Bowers, 1990). The structure and modulation by vertical mixing (mainly the springs-neaps tidal cycle) of the gravity currents and the corresponding restitution flow tend to maintain the cyclonic circulation in the UGC.

The residual circulation in the UGC was first inferred by Alvarez-Borrego and Galindo-Bect (1974), who showed that the surface distribution pattern of the hydrographic variables T, S, and σ_t was consistent with a cyclonic residual circulation. Although it is reasonable to assume a residual horizontal circulation based on the distributions of these properties, there are other factors to take into consideration. Our results show that the circulation in the UGC is influenced by the circulation in the NGC. This is most evident during the cyclonic period, when the UGC circulation is clearly a continuation of the NGC circulation. From June to September, the winds in the NGC blow northward (Zamudio, Metzger, and Hogan, 2011), aiding a northwestward current that penetrates into the UGC from the continental side. From November to February, the NGC is characterized by a generally southeastward-directed wind, which opposes the propagation of the poleward current, weakening the cyclonic circulation in the NGC and hence its influence on the circulation in the UGC.

Lateral Structure of the Exchange Flow

The currents entering the UGC from the NGC are affected by the high evaporation rate, well-mixed conditions, and stratification in the UGC, resulting in an exchange pattern with both vertical and horizontal shear.

This exchange pattern between the UGC and the NGC is consistent with an inverse estuarine circulation forced by density gradients (Largier, 2010; Nunes-Vaz, Lennon, and Bowers, 1990; Valle-Levinson, 2011). The circulation resulting from density gradients consists of a net outflow near the bottom and a net inflow at the surface (*i.e*. a net volume inflow into the UGC that is lost by net evaporation). These density-induced inflows and outflows may be influenced by basin width, friction, and Earth's rotation and can be characterized as a function of the Kelvin (K_e) and Ekman (E_k) numbers (Valle-Levinson, 2008).

The Kelvin number is a nondimensional number that compares the basin width (B) with the internal Rossby radius of deformation (R_i) (*i.e.* $K_e = B/R_i$, where $R_i = (g'h)^{1/2}/f$, g' is the reduced gravity, h is the depth of the buoyant part of the density-induced flow, and f is the Coriolis parameter). Assuming $R_i \sim 31$ km (Lavín and Marinone, 2003; Lavín *et al*., 1997) and taking $B = 80$ km gives a Kelvin number $K_e = 2.71$. The Kelvin number represents the nondimensional dynamic width of the system. In wide systems, such as the UGC ($K_e > 2$), the exchange flow is laterally sheared.

On the other hand, the Ekman number (also nondimensional) compares the Earth's rotational effects (Coriolis) with the frictional effects (*i.e.* $E_k = A_z/fH^2$, where A_z is the vertical eddy viscosity, f is the Coriolis parameter, and H is the maximum depth). Assuming that $A_z = 3 \times 10^{-4}$ m^2/s (Lavín, Godínez, and Alvarez, 1998), $f = 7.62 \times 10^{-5}$ 1/s (calculated at 31°N), and $H = 52$ m as the maximum depth, we obtain an Ekman number $E_k = 0.0014$. The Ekman number is the nondimensional dynamic depth of the system. Low values of E_k imply that frictional effects are restricted to a thin bottom boundary layer (*i.e*. the flow becomes nearly geostrophic and depends on the dynamic width of the system).

The exchange flows previously described may be closely related to currents generated by the water mass formation process in inverse estuaries, such as South Australian gulfs, which have similar physical characteristics to the UGC (de Silva Samarasinghe, 1998; Nunes-Vaz, Lennon, and Bowers, 1990). The water mass formation in the UGC was previously discussed by Lavín, Godínez, and Alvarez (1998), whose proposed mechanism is that the excess of evaporation produces high salinities and hence an increment in density toward the head of the UGC, resulting in denser and saltier water flowing under (outward), which is replaced by less dense water flowing at the surface (inward). This mechanism is reflected in the horizontal and vertical distribution of the hydrographic variables presented in Figure 9 and is consistent with the circulation and exchange flow patterns proposed in this work.

CONCLUSIONS

The seasonal salinity and heat balance in the UGC were studied by using hydrographic data from 24 cruises and meteorological data obtained from the ERA-Interim reanalysis.

We found that evaporation always exceeds precipitation in the UGC, with an annual average of 0.81 m/y. The net excess of evaporation over the year was shown to produce a net excess of salinity, mainly in the shallower part of the UGC; this excess of salinity has to be exported into the NGC to attain balance. Consequently, the UGC exports salinity to the NGC almost all year. The horizontal salinity flux reaches its maximum in November (~5 g/kg per year), with an annual mean of 1.60 g/kg per year.

The highest salinity values were found in the shallower part, where the annual component is dominant; lower salinity was found in the deepest part of the UGC, where both annual and

semiannual signals are equally important and closer to the seasonal behavior of the NGC.

The UGC gains heat from the surface most of the year at an average of 70 W/m^2. As with the salinity, the excess of heat must also be exported into the NGC; hence, the UGC exports its heat content for most of the year. The horizontal heat flux reaches a maximum of ~0.45 TW in October and has an annual mean of 0.16 TW. The difference in temperature between domains (*i.e.* the temperature gradient in the UGC) is less defined than that in salinity, and the annual component dominates the temperature variability in all domains.

The calculation of advective plus diffusive fluxes with the use of balance equations helped provide a clear outline of the factors that influence the seasonal exchange of salinity and heat content between the UGC and the NGC. However, it should be emphasized that a better data set of temperature and salinity is needed to refine the analysis and reduce errors.

We used a high-resolution nested ROMS model configuration to reproduce circulation in the UGC. The results of the simulation indicate that the model reproduces well the expected inverse estuarine circulation of the UGC: a mainly cyclonic circulation at the surface, which is also presented in the vertical distribution as a laterally sheared flow pattern. This circulation is a common feature in wide inverse estuaries, in which the circulation is forced by density gradients (gravitational circulation) caused by high evaporation rates that are influenced by the Coriolis effect. Although the gravitational circulation events last only a few days, they play an important role in the residual circulation of the UGC, and therefore on flushing and residence time, in the balances of heat and salt, and in the transport of nutrients, larvae, and sediments. Finally, it is necessary to clarify that although the interannual variability is important in the Northern Gulf of California, it is outside the scope of this work. One of the major limitations is the temporal and spatial availability of *in situ* data. We believe that an important follow-up investigation needs to address this later variability.

ACKNOWLEDGMENTS

This work was funded by the National Council of Science and Technology (CONACYT) grant SB-2009-133708. Scholarships were awarded to J.M. by CONACYT (reg. 203842), Ensenada Center for Scientific Research and Higher Education (CICESE) and the David and Lucile Packard Foundation through the University of Arizona PANGAS project. We thank two anonymous reviewers for their insightful comments that helped improve this work.

LITERATURE CITED

Alvarez-Borrego, S.; Flores-Báez, B.P., and Galindo-Bect, L.A., 1975. Hidrología del Alto Golfo de California II. Condiciones durante invierno, primavera y verano. *Ciencias Marinas*, 2(1), 21–36.

Alvarez-Borrego, S. and Galindo-Bect, L.A., 1974. Hidrología del Alto Golfo de California-I. Condiciones Durante Otoño. *Ciencias Marinas*, 1(1), 46–64.

Amante, C. and Eakins, B., 2009. ETOPO1 1 Arc-Minute Global Relief Model: Procedures, Data Sources and Analysis. National Geophysical Data Center, *NOAA Technical Memorandum, NOAA/NESDIS-24*. doi:10.7289/V5C8276M

Argote, M.L.; Amador, A.; Lavín, M.F., and Hunter, J.R., 1995. Tidal dissipation and stratification in the Gulf of California. *Journal of Geophysical Research: Oceans (1978–2012)*, 100(C8), 16103–16118.

Beardsley, R.C.; Limburner, R., and Rosenfeld, L., 1985. Introduction, CODE-2 moored array and large scale data report. *Woods Hole Oceanographic Institute Technical Report WHOI 85-35*, 234p.

Beron-Vera, F.J.; Ochoa, J., and Ripa, P., 1999. A note on boundary conditions for salt and freshwater balances. *Ocean Modelling*, 1(2), 111–118.

Beron-Vera, F.J. and Ripa, P., 2000. Three-dimensional aspects of the seasonal heat balance in the Gulf of California. *Journal of Geophysical Research: Oceans (1978–2012)*, 105(C5), 11441–11457.

Beron-Vera, F.J. and Ripa, P., 2002. Seasonal salinity balance in the Gulf of California. *Journal of Geophysical Research: Oceans (1978–2012)*, 107(C8), 15-1–15-15.

Bray, N.A., 1988a. Thermohaline circulation in the Gulf of California. *Journal of Geophysical Research*, 93(C5), 4993–5020.

Bray, N.A., 1988b. Water mass formation in the Gulf of California. *Journal of Geophysical Research: Oceans (1978–2012)*, 93(C8), 9223–9240.

Carrillo, L.; Lavín, M.F., and Palacios-Hernández, E., 2002. Seasonal evolution of the geostrophic circulation in the northern Gulf of California. *Estuarine, Coastal and Shelf Science*, 54(2), 157–173.

Carton, J.A. and Giese, B.S., 2008. A reanalysis of ocean climate using simple ocean data assimilation (SODA). *Monthly Weather Review*, 136(8), 2999–3017. doi:10.1175/2007MWR1978.1

Casey, K.; Brandon, T.; Cornillon, P., and Evans, R., 2010. The past, present and future of the AVHRR pathfinder SST program. *In:* Barale, V.; Gower, J., and Alberotanza, L. (eds.), *Oceanography from Space: Revisited*. London: Springer, pp. 273–288.

Castro, R.; Lavín, M.F., and Ripa, P., 1994. Seasonal heat balance in the Gulf of California. *Journal of Geophysical Research: Oceans (1978–2012)*, 99(C2), 3249–3261.

de Silva Samarasinghe, J.R., 1998. Revisiting Upper Gulf St Vincent in South Australia: The Salt Balance and its Implications. *Estuarine, Coastal and Shelf Science*, 46(1), 51–63.

de Silva Samarasinghe, J.R. and Lennon, G.W., 1987. Hypersalinity, flushing and transient salt-wedges in a tidal gulf-an inverse estuary. *Estuarine, Coastal and Shelf Science*, 24(4), 483–498.

ECMWF (European Centre for Medium-Range Weather Forecasts), 2010. http://apps.ecmwf.int/datasets/.

Egbert, G.D. and Erofeeva, S.Y., 2002. Efficient inverse modeling of barotropic ocean tides. *Journal of Atmospheric and Oceanic Technology*, 19(2), 183–204.

Krauss, W., 1973. *Methods and Results of Theoretical Oceanography, Volume 1: Dynamics of the Homogeneous and the Quasihomogeneous Ocean*. Berlin: Borntraeger, 302p.

Large, W.G.; McWilliams, J.C., and Doney, S.C., 1994. Oceanic vertical mixing: A review and a model with a nonlocal boundary layer parameterization. *Reviews of Geophysics*, 32(4), 363–403. doi:10.1029/94RG01872

Largier, J., 2010. Low-inflow estuaries: Hypersaline, inverse, and thermal scenarios. *In:* Valle-Levinson, A. (ed.), *Contemporary Issues in Estuarine Physics*. Cambridge, U.K.: Cambridge University Press, pp. 247–272.

Lavín, M.F.; Durazo, R.; Palacios, E.; Argote, M.L., and Carrillo, L., 1997. Lagrangian observations of the circulation in the northern Gulf of California. *Journal of Physical Oceanography*, 27(10), 2298–2305.

Lavín, M.F.; Gaxiola-Castro, G.; Robles, J.M., and Richter, K., 1995. Winter water masses and nutrients in the northern Gulf of California. *Journal of Geophysical Research: Oceans (1978–2012)*, 100(C5), 8587–8605.

Lavín, M.F.; Godínez, V.M., and Alvarez, L.G., 1998. Inverse-estuarine features of the Upper Gulf of California. *Estuarine, Coastal and Shelf Science*, 47(6), 769–795.

Lavín, M.F. and Marinone, S.G., 2003. An overview of the physical oceanography of the Gulf of California. *In:* Fuentes, O.; Sheinbaum, J., and Ochoa, J. (eds.), *Nonlinear Processes in Geophysical Fluid Dynamics: A Tribute to the Scientific Work of Pedro Ripa*. Dordrecht, The Netherlands: Springer, pp. 173–204.

Lavín, M.F. and Organista, S., 1988. Surface heat flux in the northern Gulf of California. *Journal of Geophysical Research: Oceans (1978–2012)*, 93(C11), 14033–14038.

Lavín, M.F. and Sánchez, S., 1999. On how the Colorado River affected the hydrography of the Upper Gulf of California. *Continental Shelf Research*, 19(12), 1545–1560.

Marinone, S.G., 2003. A three-dimensional model of the mean and seasonal circulation of the Gulf of California. *Journal of Geophysical Research: Oceans (1978–2012)*, 108(C10), 3325. doi:10.1029/2002JC001720

Marinone, S.G.; Lavín, M.F., and Parés-Sierra, A., 2011. A quantitative characterization of the seasonal Lagrangian circulation of the Gulf of California from a three-dimensional numerical model. *Continental Shelf Research*, 31(14), 1420–1426.

McDougall, T.J. and Barker, P.M., 2011. Getting Started with TEOS-10 and the Gibbs Seawater (GSW) Oceanographic Toolbox, 28p., SCOR/IAPSO WG127, ISBN 978-0-646-55621-5.

Mesinger, F.; DiMego, G.; Kalnay, E.; Mitchell, K.; Shafran, P.C.; Ebisuzaki, W.; Jović, D.; Woollen, J.; Rogers, E.; Berbery, E.H.; Ek, M.B.; Fan, Y.; Grumbine, R.; Higgins, W.; Li, H.; Lin, Y.; Manikin, G.; Parrish, D., and Shi, W., 2006. North American regional reanalysis. *Bulletin of the American Meteorological Society*, 87(3), 343–360. doi:10.1175/BAMS-87-3-343

Nunes-Vaz, R.A.; Lennon, G.W., and Bowers, D.G., 1990. Physical behaviour of a large, negative or inverse estuary. *Continental Shelf Research*, 10(3), 277–304.

Paden, C.A.; Winant, C.D., and Abbott, M.R., 1993. Tidal and atmospheric forcing of the upper ocean in the Gulf of California: 2. Surface heat flux. *Journal of Geophysical Research: Oceans (1978–2012)*, 98(C11), 20091–20103.

Palacios-Hernández, E.; Beier, E.; Lavín, M.F., and Ripa, P., 2002. The effect of the seasonal variation of stratification on the circulation of the northern Gulf of California. *Journal of Physical Oceanography*, 32(3), 705–728.

Penven, P.; Marchesiello, P.; Debreu, L., and Lefèvre, J., 2008. Software tools for pre- and post-processing of oceanic regional simulations. *Environmental Modelling & Software*, 23(5), 660–662. doi:10.1016/j.envsoft.2007.07.004

Sánchez-Velasco, L.; Lavín, M.F.; Jiménez-Rosenberg, S.P.A.; Montes, J.M., and Turk-Boyer, P.J., 2012. Larval fish habitats and hydrography in the Biosphere Reserve of the Upper Gulf of California (June 2008). *Continental Shelf Research,* 33(C), 89–99.

Valle-Levinson, A., 2008. Density-driven exchange flow in terms of the Kelvin and Ekman numbers. *Journal of Geophysical Research*, 113(C4), C04001. doi: 10.1029/2007JC004144

Valle-Levinson, A., 2011. Classification of estuarine circulation. *In*: Wolanski, E. and McLusky, D. (eds.), *Treatise on Estuarine and Coastal Science*, Volume 1. Waltham, Massachusetts: Academic Press, pp. 75–86.

Wessel, P. and Smith, W.H.F., 1996. A global, self-consistent, hierarchical, high-resolution shoreline database. *Journal of Geophysical Research*, 101(B4), 8741–8743. doi:10.1029/96JB00104

Woodruff, S.D.; Slutz, R.J.; Jenne, R.L., and Steurer, P.M., 1987. A comprehensive ocean-atmosphere data set. *Bulletin of the American Meteorological Society*, 68(10), 1239–1250.

Zamudio, L.; Metzger, E.J., and Hogan, P., 2011. Modeling the seasonal and interannual variability of the northern Gulf of California salinity. *Journal of Geophysical Research*, 116(C2), C02017. doi:10.1029/2010JC006631